Special Collection

Tailoring Preferential Orientation in $BaTiO_3$-based Thin Films from Aqueous Chemical Solution Deposition

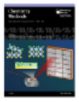

Kristine Bakken,[a] Anders B. Blichfeld,[a] Inger-Emma Nylund,[a] Dmitry Chernyshov,[b] Julia Glaum,[a] Tor Grande,[a] and Mari-Ann Einarsrud*[a]

Ferroelectric properties of thin films can be enhanced by crystallographic texture. In this work, we report on how heat treatment of films can be designed to tailor the degree of preferential orientation in $BaTiO_3$-based thin films from aqueous chemical solution deposition. In situ synchrotron X-ray diffraction in combination with Rietveld refinements was used to study the crystallization process of films from a single deposition and to give an in-depth characterization of the crystallographic texture of the films. Transmission electron microscopy was employed to evaluate the microstructure and degree of preferred orientation in thicker films from multiple depositions. Texture was induced in the multilayer films by a repeated annealing process. Cube-on-cube growth was demonstrated to occur in both single and multi-layered films provided the heating program was designed to give limited nucleation and growth below the threshold for where cube-on-cube growth is favoured, resulting in a very high degree of preferred orientation. The cube-on-cube grown films were relaxed with respect to the lattice unit cell mismatch between the film and the substrate, where the relaxation of stress depends on the film thickness. Texture and cube-on-cube growth were demonstrated on several types of single-crystal oxide substrates. Calcium and zirconium substitution did not alter the crystallization process, but zirconium slowed down the texture formation kinetics. The ferroelectric response was strongest in the films with a high degree of preferred orientation.

1. Introduction

For most of the typical applications, it is beneficial to use piezo- or ferroelectric materials as thin films, as the piezo- and ferroelectric response is enhanced in films with texture or epitaxy. Smaller devices, lower operating voltage, higher speed and lower processing temperatures are some additional advantages.[1] Flexible energy harvesters, multilayer ceramic capacitors, nanogenerators and in vivo sensors are new possible applications where ferroelectric thin films are attractive. Hence, sustainable and simple deposition routes to high quality films with a high degree of crystallographic texture need to be developed in order to fully utilize the potential of the materials.[2] Chemical solution deposition (CSD) is a well-suited, inexpensive and flexible method for fabrication of oxide thin films on an industrial scale.[3] The synthesis approach is simple, as a stable precursor solution with the desired metal ions is deposited onto a substrate by for example by spin coating before thermal processing of the film. Depending on the precursor solution chemistry and the heating profile used, different pyrolysis and crystallization reactions occur. Aqueous precursor solutions remove the need for toxic organic solvents and simplify the process as an inert atmosphere is not required.[3b]

$BaTiO_3$ is the prototypic ferroelectric oxide, widely used in ceramic capacitors and well-studied, as this material system is suitable for tailoring the material properties through doping and cation substitution. The substitution with small amounts of Ca was reported to increase the T_C, with a maximum of 136 °C for $Ba_{0.92}Ca_{0.08}TiO_3$,[4] which is uncommon for the $BaTiO_3$-system as most solid solutions decease the Curie temperature. Another compound that has gained interest is $Ba_{0.85}Ca_{0.15}Zr_{0.1}Ti_{0.9}O_3$ (BCZT), where the co-substitution on both the A- and B-sites results in a high d_{33}-value,[5] but this is heavily dependent on the processing.[2b] $BaTiO_3$-based thin films produced by CSD generally have polycrystalline or columnar microstructures, where the latter results from homoepitaxial growth of consecutive layers.[3a,6] As formation of the perovskite phase occurs either through the solid-state reaction of $BaCO_3$ and TiO_2 or through the decomposition of an intermediate oxycarbonate phase, nucleation will occur homogeneously throughout the film. The columnar microstructure was observed by Hasenkox et al.[6c] and Hoffmann et al.[6d] to be dependent on the precursor concentration, as homoepitaxial growth could only be supported in thin layers on Pt/Si substrate. Highly oriented columnar $BaTiO_3$ films on $LaAlO_3$ (LAO) were prepared by Schwartz et al.[6e] utilizing a $BaTiO_3$ seed layer annealed at high

[a] Dr. K. Bakken, Dr. A. B. Blichfeld, I.-E. Nylund, Prof. J. Glaum, Prof. T. Grande, Prof. M.-A. Einarsrud
Department of Materials Science and Engineering
NTNU Norwegian University of Science and Technology
Trondheim (Norway)
E-mail: mari-ann.einarsrud@ntnu.no
[b] Dr. D. Chernyshov
Swiss-Norwegian Beamlines
European Synchrotron Radiation Facility
Grenoble (France)

Supporting information for this article is available on the WWW under https://doi.org/10.1002/cmtd.202100064

Special Collection

Part of a Special Collection on In Situ and Operando Time-Resolved X-Ray and Neutron Diffraction Studies. Please visit chemistry-methods.org/collections to view all contributions.

temperature (1100 °C) and annealing of the final film at high temperature for 30–120 min. Textured films were also prepared on Si substrates, using $La(NO_3)_3$ buffer layers to increase adhesion and a heating rate of 300 °C/min, resulting in films with equiaxed grains.[7] Highly oriented $BaTiO_3$ films following the substrate orientation were also reported on Pt coated (100)-, (110)- and (111)-MgO substrates.[8] The films were dense and seemingly free of grain boundaries and TEM investigation showed an epitaxial orientation relationship between the films and substrates.[8] Epitaxial $BaTiO_3$ films on Si-substrates with a 2 nm (100)-$SrTiO_3$ (STO) interface layer are also reported, with dense grain-like microstructure after annealing at 600 °C for 1 h.[9] Moreover, epitaxial BCZT was grown with columnar grains on a $La_{0.5}Sr_{0.5}CoO_3/CeO_2/Y_{0.15}Zr_{0.85}O_{1.93}$/Si layered structure[10] and with a grain-like microstructure on $La_{0.7}Sr_{0.3}MnO_3$-coated STO.[11] Preparation of textured BCZT films have also been reported, where the use of $LaNiO_3$ buffer layer increased the (100) preferred orientation and the ferroelectric response compared to films prepared directly on Pt/Si.[12]

Few descriptions on the preparation of BaTiO3 thin films by aqueous CSD are reported in literature. Ræder et al.[13] fabricated BaTiO3 films using a water-based approach, followed by our previous work,[14] where preparation of polycrystalline,[14] textured,[14] and relaxed epitaxial $BaTiO_3$ thin films were demonstrated.[13,15] In the latter case, in-plane ferroelectric properties[13,15a] and TEM imaging on different orientations of STO substrates[15b] were reported. By in situ X-ray diffraction, the mechanisms for formation of texture in single layered (20–30 nm) $BaTiO_3$ thin films was shown to be related to the structure of the intermediate phases present before the perovskite formed, while slow heating enhanced the degree of preferred orientation.[14] The intermediate phases were determined to consist of small poorly crystalline regions of $BaCO_3$ with a calcite structure and $BaTi_4O_9$, by a combination of in situ X-ray total scattering, infrared spectroscopy and electron microscopy.[16] Based on this work, Khomyakova et al. recently developed a CSD synthesis for polycrystalline BCZT thin films.[17]

The combination of in situ studies during decomposition and crystallization with ex situ characterization techniques demonstrate the potential for uncovering the mechanisms behind the complex chemical reaction occurring during annealing of thin films prepared by CSD. This understanding can be expanded using in situ characterization tools and is crucial for tailoring film properties. However, the focus has so far not been on understanding the crystallization process and how this can be tailored to achieve texture, especially for multi-layered $BaTiO_3$ thin films, or how these mechanisms are impacted by cation substitution and type of substrate.

Here we report on guidelines for how to design the film annealing to tailor the degree of preferred orientation in $BaTiO_3$-based thin films from aqueous CSD. The mechanisms for achieving a high degree of texture and cube-on-cube growth in both single and multi-layered $BaTiO_3$-based thin films are discussed. Moreover, the preferred orientation in the textured films and how that is affected by the substrate is investigated, and stress relaxation in the cube-on-cube grown films was characterized. In situ synchrotron X-ray diffraction and electron microscopy was used to study $BaTiO_3$, $Ba_{0.92}Ca_{0.08}TiO_3$ (BCT) and $Ba_{0.85}Ca_{0.15}Zr_{0.1}Ti_{0.9}O_3$ (BCZT) thin films on various single-crystal substrates. Furthermore, the in-plane ferroelectric response was measured. The texture in the films was observed to adhere to the substrate orientation. Moreover, it is proposed that the cube-on-cube growth mode demonstrated for the $BaTiO_3$-based films is available for other oxide films on suitable substrates, provided limited homogeneous nucleation occurs before exceeding the threshold for cube-on-cube growth.

Experimental Section

Synthesis

The preparation of the aqueous precursor solution has been reported previously.[13–14,17] Separate Ba-, Ca-, Zr- and Ti-complex solutions were prepared and then mixed in stochiometric ratios to make final $BaTiO_3$, $Ba_{0.92}Ca_{0.08}TiO_3$ (BCT) and $Ba_{0.85}Ca_{0.15}Zr_{0.1}Ti_{0.9}O_3$ (BCZT) precursor solutions with concentrations of 0.26 M, 0.25 M and 0.23 M respectively. For deposition of multilayer films the precursor solutions were diluted with deionized water to 0.13 M. $Ba(NO_3)_2$ (98%, Sigma-Aldrich, St. Louis, MO, USA) and $Ca(NO_3)_2 \cdot xH_2O$ (99%, Sigma-Aldrich, St. Louis, MO, USA) were stabilized in water with both EDTA (99.9%, Sigma-Aldrich, St. Louis, MO, USA) and citric acid (99.5%, Sigma-Aldrich, St. Louis, MO, USA), while Ti-isopropoxide (97%, Sigma-Aldrich, St. Louis, MO, USA) and $ZrO(NO_3)_2 \bullet x\ H_2O$ (99%, Sigma-Aldrich, St. Louis, MO, USA) were stabilized with citric acid, and ammonia solution (30%, Sigma-Aldrich, St. Louis, MO, USA) was used to adjust the pH of the solutions to neutral prior to mixing. For the multilayer film deposition, the precursor solutions were diluted to half the prepared concentration by addition of water.

Selected substrates (1 × 1 cm) were used for the thin film fabrication and an overview of the films prepared are provided in Table 1. All substrates were washed with ethanol (96%) and ISO 5 clean room wipes before they were cleaned with oxygen plasma (Femto, Diener Electronic GmbH + Co, Ebhausen, Germany) for 2 min to enhance wetting. The precursor solution was deposited onto the substrate through a syringe with a 0.2 mm cellulose acetate membrane filter and then spin coated (WS-400B-6NPP-LITE/AS, Laurell Technologies, Montgomery, PA, USA) at 3500 rpm for 30 s. Afterwards the films were dried on a hotplate for 4 min at 180 °C. The films were heated on a rapid heating plate (RHP) described in detail by Blichfeld et al.,[18] either during the in situ synchrotron X-ray diffraction experiments or in a fume hood for the multi-layer films. For the multi-layered films, each layer was fully crystallized before the next was deposited. All films were annealed in air and cooled by switching off the heat source.

Characterization

Synchrotron X-ray diffraction (XRD) on the thin films was conducted at the BM01 end-station, Swiss-Norwegian Beamlines (SNBL) at ESRF (The European Synchrotron Radiation Facility, Grenoble, France). The films were characterized at two separate beamtimes using wavelengths of 0.78449 Å and 0.77624 Å, chosen as to limit fluorescence from Sr from the STO substrates. A Pilatus2M 2D-detector was used[19] and the films were heated in situ on a set up described in detail by Blichfeld et al.[18] The experimental details and the procedure for data treatment of the in situ data are outlined in Blichfeld et al.[18] and Bakken et al.,[14] (a schematic overview of the setup is shown in Figure S1 in the Supporting

Table 1. Overview of thin films investigated, showing film number, substrate, thickness and annealing conditions for the various $BaTiO_3$-based films. Multilayer films are marked in bold.

Film number	Film/Substrate	#Layers/ Total film thickness [nm]	Heating	Figure number
1	$BaTiO_3$/(100)-STO	1/25	0.1 °C s^{-1} up to 700 °C hold for 60 min	Figure 1(a–c) & Figure 2
2	$BaTiO_3$/(110)-STO	1/25	0.2 °C s^{-1}s up to 700 °C hold for 30 min	Figure 1(d–f)
3	$BaTiO_3$/(111)-STO	1/25	0.2 °C s^{-1} up to 700 °C hold for 30 min	Figure 1(g–i)
4	$BaTiO_3$/(100)-STO	1/25	4 °C s^{-1} up to 560 °C hold for 10 min, 1 °C s^{-1} up to 1000 °C hold for 15 min	Figure 3(a)
5	$BaTiO_3$/(100)-STO	1/25	5 °C s^{-1} up to 560 °C hold for 5 min, 10 °C s^{-1} up to 965 °C hold for 15 min	Figure 3(c)
6	$BaTiO_3$/(100)-STO	1/25	20 °C s^{-1} up to 700 °C, 5 °C s^{-1} up to 1000 °C hold for 15 min	Figure 3(e), Figure 4, Figure 5
7	$BaTiO_3$/(100)-STO	15/180	1.5 °C s^{-1} up to 455 °C, 0.67 °C s^{-1} up to 588 °C, 5 °C s^{-1} up to 1000 °C hold for 5 min	Figure 6, Figure 8 (Fast-1000 °C)
8	$BaTiO_3$/(100)-STO	15/193	1.5 °C s^{-1} up to 455 °C, 0.67 °C s^{-1} up to 588 °C, 5 °C s^{-1} up to 700 °C hold for 5 min	Figure 7, Figure 8 (Fast-700 °C)
9	$BaTiO_3$/(100)-STO	15/206	0.2 °C s^{-1} up to 700 °C annealed for 5 min	Figure 8, Figure S8 (Slow-700 °C)

Information). In short, the films were measured in grazing incidence and thermal expansion of the setup was compensated by sequentially offsetting the height during data recording, followed by postprocessing the data based on the signal from the substrate and thermal expansion coefficients from literature. The preliminary data processing and inspection of the powder diffraction profiles was done with BM01 software tools, such as BUBBLE[19] and MEDVED.[20] For the texture refinements the diffractograms were integrated with the BUBBLE software[19] with azimuthal slicing of 5°, to preserve the texture information. The substrate reflections were masked, and a background function subtracted prior to refinements (Figure S1(b) in the Supporting Information). Rietveld refinements were preformed using the MAUD (Materials Analysis Using Diffraction) software (v 2.93)[21] with the E-WIMV model to account for texture. No symmetry was imposed for the texture, and the refinements were run to convergence. The calculated orientation distribution function (ODF) was exported from MAUD and pole figures based on the ODFs were calculated with the MTEX package (v 5.2.4)[22] for MATLAB (v R2018a) assuming a cubic structure for the films. Texture was also visualized by slicing the data in two orthogonal angular directions; tilt (ω) and azimuthal (η). These data were measured with stepwise increasing tilt. The ω-series was integrated to 1D diffractograms with the BUBBLE software without any mask. The azimuthal series was made by summing the ω-series into one single 2D diffractogram and integrated with azimuthal 0.5° slicing.

Electrical characterization was conducted as described in Refs. [13, 15a, 23]. Interdigitated electrodes were patterned using a lift-off process based on ma-N 440-series photoresist (micro resist technology GmbH, Berlin, Germany) exposed by a MLA 150 maskless aligner (Heidelberg Instruments Mikrotechnik GmbH, Heidelberg, Germany). Ti (5 nm) and Pt (20 nm) were deposited using e-beam evaporation (ATC series, AJA international) to form the electrodes. The thin films with the electrodes were annealed in air at 600 °C for 2 h with heating and cooling rates of 200 °C h^{-1}. Finally, the samples were cleaned in isopropanol using ultrasound for 2 min. The IDEs had an electrode spacing of ~7.37 μm, electrode width of ~2.63 μm, and 100 fingers with 900 μm overlap. Electrical characterization was performed on a TF analyzer 2000 (aixACCT Systems GmbH, Aachen, Germany) using a thin film sample holder with integrated heating element and thermometer. The maximum electric field applied to the films were 20 kV cm^{-1} with a frequency of 30 Hz.

Scanning electron microscopy (SEM) of the thin films was performed using a field-emission FE-SEM Zeiss Ultra 55 LE microscope (Carl Zeiss AG, Oberkochen, Germany) with an in-lens detector. No coating was applied to the samples prior to imaging. Transmission electron microscopy (TEM) was performed on crystalline 15-layer films. One cross-sectional TEM specimen was made from each film using a focused ion beam (Helios G4 UX, Thermo Fisher Scientific, Waltham, MA, USA). The chosen area was first coated with a carbon protection layer applied in two steps, first a thin layer using the electron beam, then a thicker layer using the ion beam. The lift-out and initial thinning of the sample was done using the ion beam at 30 kV, while the final thinning steps were done at 5 kV and lastly at 2 kV to make the damage layer caused by the ion beam as thin as possible. All the TEM investigations were performed on a double corrected cold FEG microscope (JEM ARM200F, JEOL Ltd., Tokyo, Japan) with an acceleration voltage of 200 kV. All the diffraction patterns were acquired using a selected area aperture with a diameter covering approximately 160 nm in real space. The high-angle annular dark-field (HAADF) STEM images were acquired using a beam convergence semi-angle of 27 mrad, and inner and outer collection angle of 119 and 471 mrad, respectively.

2. Results

2.1. The Crystallographic Texture of Single Layer $BaTiO_3$-based Films

Modified diffractograms of textured single layered $BaTiO_3$ films on different orientations of the STO substrates are shown in Figure 1, where the data was integrated as a function of the radial direction (azimuthal angle) on the detector to obtain a linear 2θ-axis. The intensity in the diffractograms was normalized on a linear scale, where the background corresponds to 0 and the most intense reflection from the sample corresponds to

Heidelberg, Germany). Ti (5 nm) and Pt (20 nm) were deposited using e-beam evaporation (ATC series, AJA international) to form the electrodes. The thin films with the electrodes were annealed in air at 600 °C for 2 h with heating and cooling rates of 200 °C h^{-1}. Finally, the samples were cleaned in isopropanol using ultrasound for 2 min. The IDEs had an electrode spacing of ~7.37 μm, electrode width of ~2.63 μm, and 100 fingers with 900 μm overlap. Electrical characterization was performed on a TF analyzer 2000 (aixACCT Systems GmbH, Aachen, Germany) using a thin film sample holder with integrated heating element and thermometer. The maximum

$BaTiO_3$ based Films

Modified diffractograms of textured single layered $BaTiO_3$ films on different orientations of the STO substrates are shown in Figure 1, where the data was integrated as a function of the radial direction (azimuthal angle) on the detector to obtain a linear 2θ-axis. The intensity in the diffractograms was normalized on a linear scale, where the background corresponds to 0 and the most intense reflection from the sample corresponds to 1. A texture component was included in the Rietveld refine-

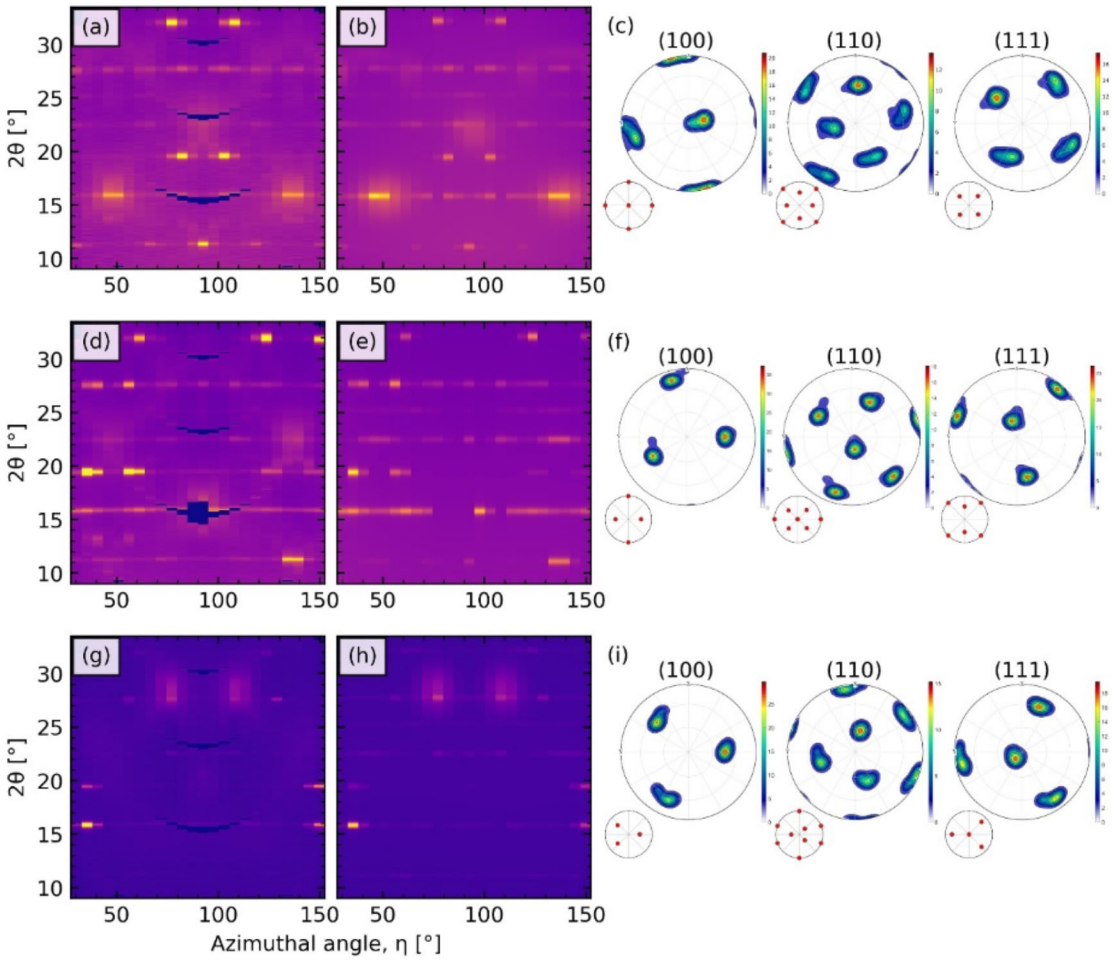

Figure 1. (a) Modified experimental and (b) refined diffractograms after refinement and (c) pole figures from Rietveld refinements for a textured 20 nm (single layer) $BaTiO_3$ film on (100)STO (Film 1). (d) Modified experimental and (e) refined diffractograms after refinement and (f) pole figures from Rietveld refinements for a textured 20 nm (single layer) $BaTiO_3$ film on (110)STO (Film 2). (g) Modified experimental and (h) refined diffractograms after refinement and (i) pole figures from Rietveld refinements for a textured 20 nm (single layer) $BaTiO_3$ film on (111)STO (Film 3). The small inserts show the theoretical pole figures for the different orientations based on a cubic unit cell (*Pm*$\bar{3}$*m*).

ments (E-WIMV model) and the substrate reflections were masked. Detailed information from the refinements are listed in Table S2 in the Supporting Information. Both the diffraction patterns and pole figures calculated from the ODFs from the texture refinements reflect the change in orientation of the STO substrate, meaning that the film texture adhere to the substrate orientation and a cubic symmetry is obtained for the film. Distortions in the pole figures relative to the theoretical pole figures could be due to tetragonality, experimental errors or a slight misalignment of the film relative to the beam. The $BaTiO_3$ film texture on (100) MgO and LAO were observed to be cubic (Figure S2 in Supporting Information), with similar diffraction patterns and pole figures as for $BaTiO_3$ on (100)-STO, showing that the film texture adheres to the substrate orientation even on different crystal lattices. The same conclusion was made for the BCT and BCZT films on (100)-STO (Figure S2 in Supporting Information), meaning that the cation substitution does not influence the preferred orientation of the film. However, the degree of preferential orientation of $BaTiO_3$ thin films on (100)-STO have been reported to increase with decreasing heating rate.[14] Considering that Zr-substitution influences both the thermodynamics and kinetics of the crystallization behaviour of BCZT compared to $BaTiO_3$ and BCT, a lower heating rate ($< 0.2\,°C\,s^{-1}$) and higher temperature ($> 600\,°C$) was necessary to achieve textured BCZT films (data not shown). However, the mechanisms for the texture formation were the same, independent of substitution.

To further study the crystallographic texture of $BaTiO_3$ on (100)-STO (Film 1), a series of diffractograms were recorded as a function of the tilt angle (incident angle) and the diffraction from a $BaTiO_3$ thin film on (100)-STO is presented in two perpendicular angular directions, tilt (ω) and azimuthal (η) in Figure 2. In the tilt direction (Figure 2(a)) the $BaTiO_3$ reflections had a spatial extension in this angular direction (horizontal lines) due to the large footprint parallel to the beam in combination with the physical size of the sample, while the

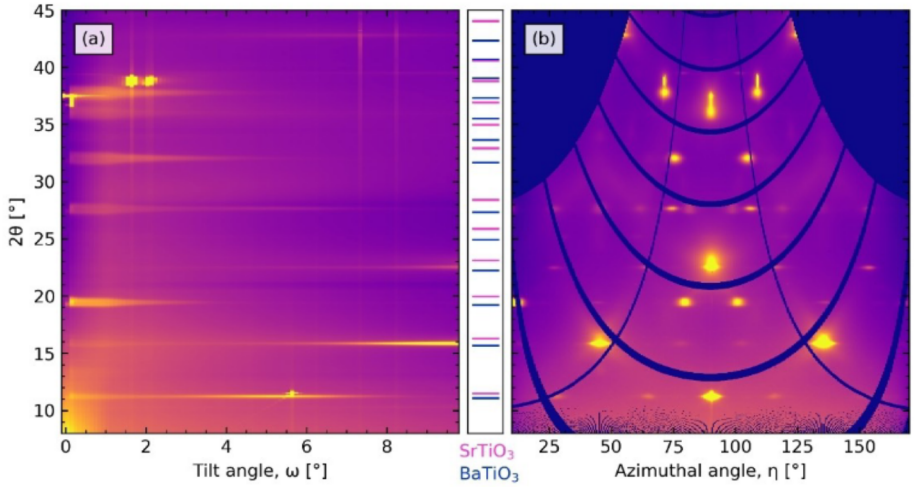

Figure 2. Diffraction from a single-layer highly textured $BaTiO_3$ thin film on (100) STO (Film 1) in two perpendicular angular directions; (a) tilt (ω) and (b) azimuthal (η). The wavelength was 0.78242 Å. Appearance of verticals lines in the tilt diffractogram in (a) are due to diffuse scattering from the substrate.

substrate reflections were distinct spots. In the azimuthal direction (Figure 2(b)) both the $BaTiO_3$ and substrate reflections are distinct diffraction spots. Although there are a series of spots in the azimuthal direction for the $BaTiO_3$ film, it is far from single crystalline like the substrate, where only a few reflections are captured by the detector for this measurement configuration. The pseudo-cubic lattice parameter of $BaTiO_3$ calculated from the (310) and (311) Bragg reflections were 4.0005 ± 0.0025 Å and 4.0068 ± 0.0025 Å, respectively, giving an average cubic lattice parameter of 4.0037 ± 0.0025 Å.

2.2. In situ X-ray Diffraction during Crystallization of Single Layer $BaTiO_3$ Thin Films

The conditions for formation of highly oriented $BaTiO_3$ thin films were investigated by in situ synchrotron XRD during crystallization of the film upon heating. Film 4 (Figure 3(a)) was heated with a hold step at 560 °C for formation of the intermediate phases (denoted "Ba-oxy") and then followed by 1 °C s^{-1} heating to 1000 °C, resulting in polycrystalline $BaTiO_3$ (denoted "Poly"). The microstructure of Film 4 after annealing (Figure 3(b)) shows the grains to be 50 nm in size distributed on the substrate with a certain degree of necking between the grains. Film 5 (Figure 3(c)), had a shorter hold step at intermediate temperature, and was then heated fast (10 °C s^{-1}) to 965 °C. Polycrystalline $BaTiO_3$ nucleated at the start of the fast heating step, but due to the fast heating the film started to transform to a highly (100)-oriented layer (seen from the decrease in peak intensities in the contour plot, denoted "Epitaxial"). Comparing Film 4 and Film 5, a fast heating rate was necessary in order to obtain the highly oriented film, meaning that a different mechanism is governing this transformation compared to the slow heating induced texture reported in Section 2.1. However, the final annealing temperature in both polycrystalline and (100)-oriented diffraction from Film 5. Complete (100)-oriented transformation was achieved in Film 6 (Figure 3(e)), due to the increased annealing temperature and fast heating (5 °C s^{-1}), demonstrating that the kinetics plays a key role in the formation of highly oriented thin films from CSD. Similar to Film 5, polycrystalline $BaTiO_3$ started to nucleate in Film 6, but most of the Bragg reflections quickly vanished as the temperature increased. The cube-on-cube relationship between the film and substrate can be seen from the appearance of a strong reflection at $2\theta = 36.7°$, right next to the (311)-STO reflections (not masked). The microstructure of Film 5 (Figure 3(d)) and Film 6 (Figure 3(f)) are distinctly different from Film 4 (Figure 3(b)), as they are continuous films with cavities instead of distributed grains. However, the holes in Film 6 (Figure 3(f)) have faceted edges, revealing the cube-on-cube growth mode for this film.

The cube-on-cube relationship of Film 6 is further illustrated by considering the reflections in the tilt diffractogram (Figure 4), which is a perpendicular direction compared to the azimuthal diffractogram shown as an insert in Figure 3(e). For the textured $BaTiO_3$ film (Film 1, Figure 2(a)), only the Bragg reflections from the substrate were confined spots, while the textured film showed horizontal diffraction lines. In contrast, in the tilt diffractogram in Figure 4 only distinct spot reflections can be seen, both from the substrate and the film. Moreover, the film is (100)-oriented, as the same reflections captured from the (100) STO substrate are present from the film, but at lower 2θ-values, due to the larger lattice parameter of $BaTiO_3$ compared to STO. Additionally, the film reflections are displaced in the tilt direction compared the substrate reflections, due to the height difference between these two diffracting layers. The (300), (310) and (311) reflections are shown in greater detail in Figure 4(b). The pseudo-cubic lattice parameters calculated from the (300), (310) and (311) $BaTiO_3$ reflections were 3.9914 ± 0.0025 Å, 4.0048 ± 0.0025 Å and 4.0356 ± 0.0025 Å, respectively.

fast heating step, but due to the fast heating the film started to transform to a highly (100)-oriented layer (seen from the decrease in peak intensities in the contour plot, denoted "Epitaxial"). Comparing Film 4 and Film 5, a fast heating rate was necessary in order to obtain the highly oriented film, meaning that a different mechanism is governing this transformation compared to the slow heating induced texture reported in Section 2.1. However, the final annealing temperature was insufficient to completely transform the film, resulting

due to the larger lattice parameter of $BaTiO_3$ compared to STO. Additionally, the film reflections are displaced in the tilt direction compared the substrate reflections, due to the height difference between these two diffracting layers. The (300), (310) and (311) reflections are shown in greater detail in Figure 4(b). The pseudo-cubic lattice parameters calculated from the (300), (310) and (311) $BaTiO_3$ reflections were 3.9914 ± 0.0025 Å, 4.0048 ± 0.0025 Å and 4.0356 ± 0.0025 Å, respectively.

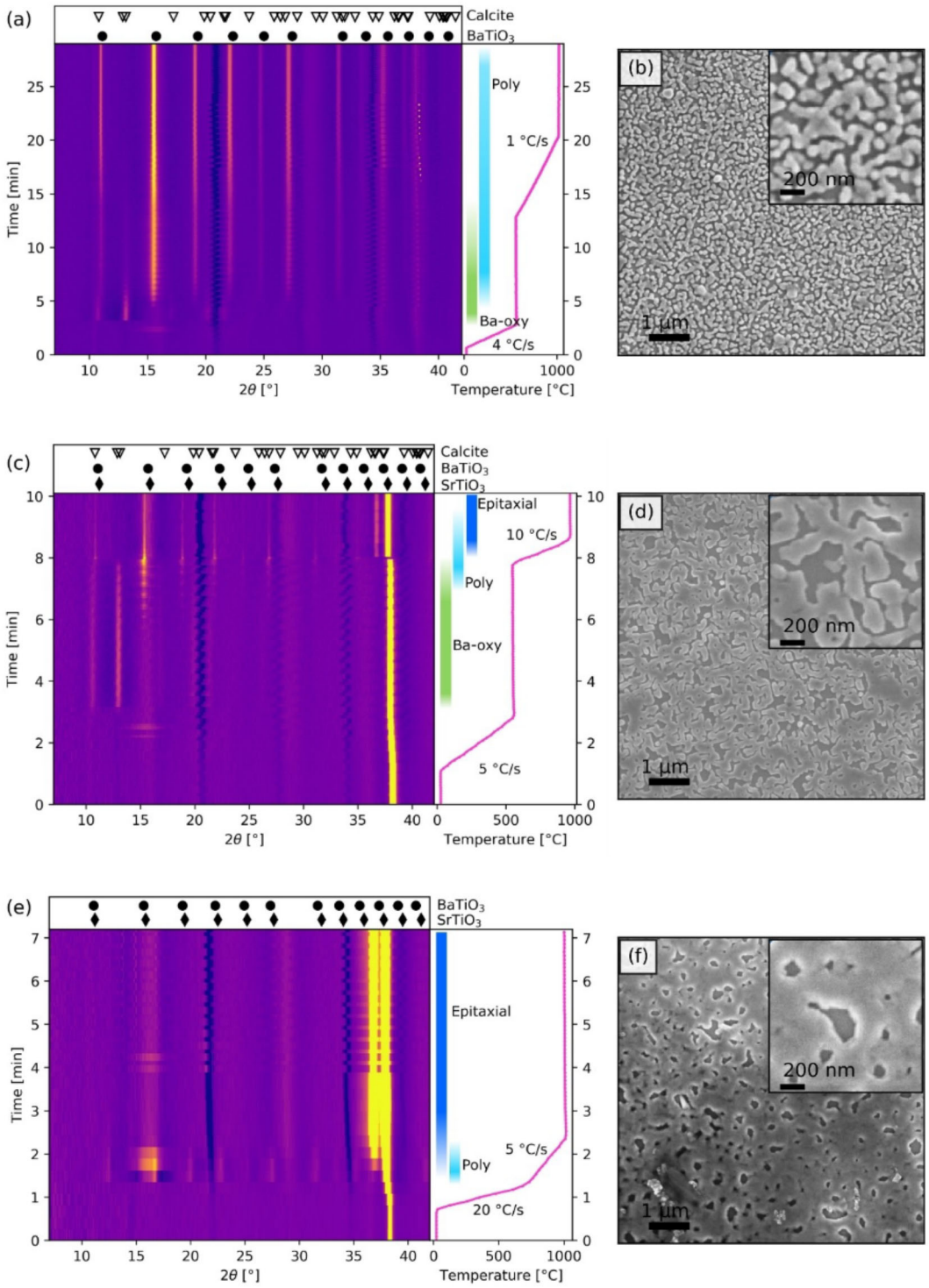

Figure 3. (a) 2D contour plot of the in situ diffractograms and temperature profile of a $BaTiO_3$ thin film on (100)STO (Film 4) as a function of time. The corresponding temperature profile with the film development is illustrated to the right. (b) Microstructure (top view) of the resulting polycrystalline $BaTiO_3$ thin film after annealing. (c) 2D contour plot of in situ diffractograms, temperature profile and (d) resulting film microstructure of a highly (100)-oriented $BaTiO_3$ thin film on (100)STO (Film 5). (e) 2D contour plot of in situ diffractograms and temperature profile of a highly (100)-oriented $BaTiO_3$ thin film on (100) STO (Film 6) and (f) resulting film microstructure. The wavelength was 0.78242 Å and apparent negative peaks are due to gaps in the detector.

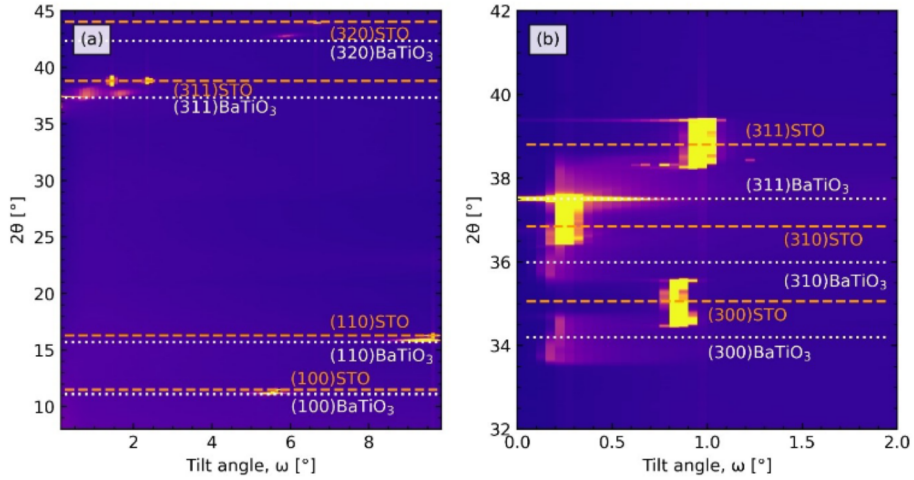

Figure 4. (a) Diffraction as a function of tilt angle for a highly oriented $BaTiO_3$ thin film on (100)-STO (Film 6) showing the cube-on-cube relationship between film and substrate. (b) Zoomed in view of the 2θ-ω area for the (300), (310) and (311) reflections.

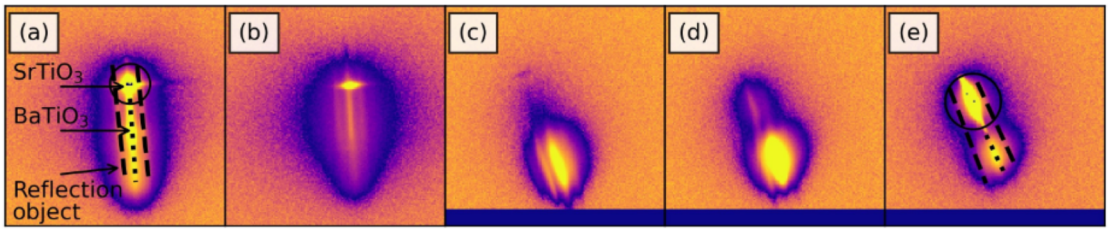

Figure 5. Cross sections of the (310) and (311) reflections for an highly (100)-oriented $BaTiO_3$ thin (Film 6) on (100)-STO. (a) (311) reflection at $\omega = 0.25°$, (b) (311) reflection at $\omega = 0.75°$, (c) (310) reflection at $\omega = 1.25°$, (d) (310) reflection at $\omega = 1.75°$ and (e) (310) reflection at $\omega = 2.25°$. Diffractograms recorded after cooling at ambient temperature.

Cross sections of the (310) and (311) reflections of Film 6 and the STO substrate (marked with black circles) are shown in Figure 5 at various tilt angles, the diffractograms were recorded 20 °C. The Bragg reflections (vertical lines in the centre) are surrounded by a cylindrical reflection object. This type of reflection object was observed for both the highly oriented films investigated in situ (Film 5 and Film 6) right after crystallization occurred. Demonstrating that the reflection objects were present already at the maximum annealing temperature (shown in the Supporting Information, Figure S3). The additional reflections correspond to a periodicity of 16.6 nm and 9.9 nm calculated from the (310) and (311) reflections respectively, arising from periodic features in the films and will be further discussed in Section 2.3.

The cube-on-cube growth mode observed for $BaTiO_3$ films on (100) STO, was also observed for $BaTiO_3$ on (110)- and (111)-STO, (100)-MgO and (100)-LAO. The microstructure of the films on STO (Figure S4) and diffractograms of the films on MgO and LAO (Figure S5 and Figure S6) are included in the Supporting Information. However, full conversion could only be achieved on STO, while the films on MgO and LAO were polycrystalline. BCT and BCZT films on (100)-STO fabricated with the same heating program as the $BaTiO_3$ films also resulted in cube-on-cube but judging from the microstructure (Figure S4 in Supporting Information), the BCT film had the same full coverage and faceted edges as the $BaTiO_3$ film, indicating that Ca-doping does not affect the crystallization. While the BCZT film had a coarser appearance, still with faceted edges, which could be due to incomplete conversion as BCZT would have a higher threshold for cube-on-cube growth compared to $BaTiO_3$.

2.3. Microstructure and Preferred Orientation in Multilayer $BaTiO_3$ Thin Films

A cross-section of a multilayer $BaTiO_3$ thin film on (100)-STO (Film 7) made by fast heating to 1000 °C, analogous to the heating program of Film 5 and Film 6, is shown in Figure 6. The film thickness was 180 nm, giving an average of 12 nm deposited per layer. The cross-section demonstrates that the film is dense and relatively homogeneous. The cross-section of the film close to the interface is displayed in Figure 6(b), where periodic dislocations were observed at the film-substrate interface with an average distance of 14.0 nm, which is close to the predicted 16.2 nm spacing for a fully relaxed film based solely on the lattice mismatch. The periodic dislocations show that the

on (100) STO, was also observed for $BaTiO_3$ on (110)- and (111)-STO, (100)-MgO and (100)-LAO. The microstructure of the films on STO (Figure S4) and diffractograms of the films on MgO and LAO (Figure S5 and Figure S6) are included in the Supporting Information. However, full conversion could only be achieved on STO, while the films on MgO and LAO were polycrystalline. BCT and BCZT films on (100)-STO fabricated with the same heating program as the $BaTiO_3$ films also resulted in cube-on-cube growth. Diffractograms of these films were not recorded

film thickness was 180 nm, giving an average of 12 nm deposited per layer. The cross-section demonstrates that the film is dense and relatively homogeneous. The cross-section of the film close to the interface is displayed in Figure 6(b), where periodic dislocations were observed at the film-substrate interface with an average distance of 14.0 nm, which is close to the predicted 16.2 nm spacing for a fully relaxed film based solely on the lattice mismatch. The periodic dislocations show that the cube-on-cube grown films investigated in this work were

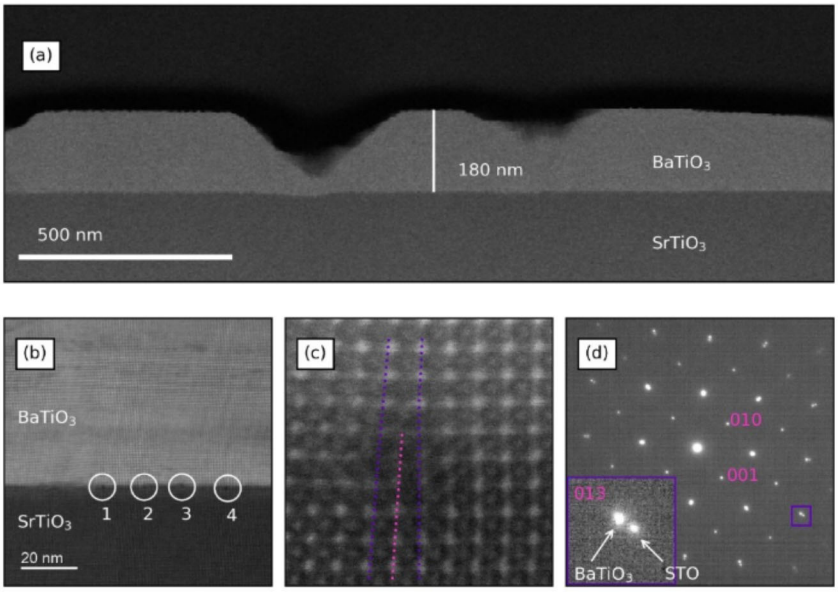

Figure 6. (a) HAADF STEM image of a cross section of a cube-on-cube grown $BaTiO_3$ thin film on (100)-STO (Film 7). (b) shows periodic dislocations at the substrate interface and (c) shows the termination of a substrate lattice plane at the film interface with an edge dislocation for dislocation marked "1". (d) Selected area diffraction patterns at the substrate-film interface. The inserts show the (013) reflection of both $BaTiO_3$ and STO.

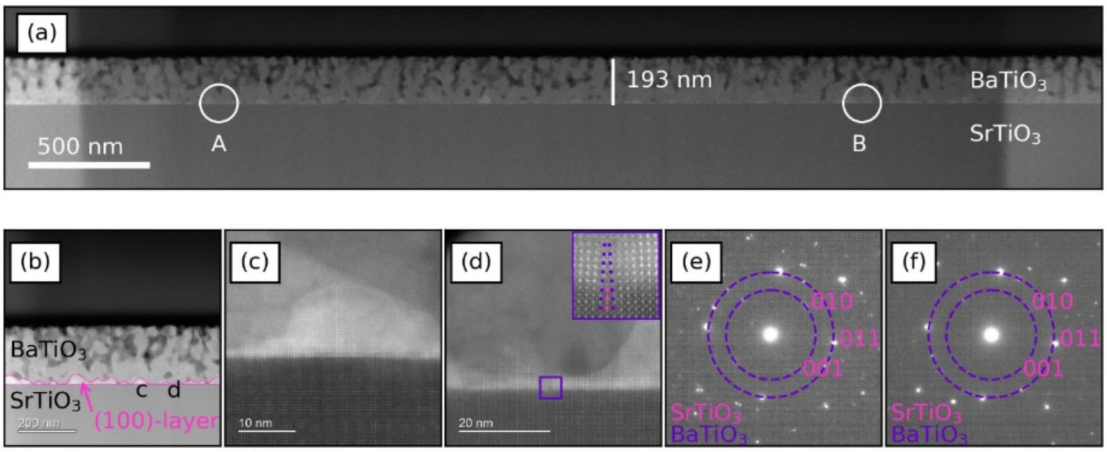

Figure 7. (a) HAADF STEM image of a cross section of a polycrystalline $BaTiO_3$ thin film on (100)-STO (Film 8). (b) The film interface in region A where the zoomed images (c) and (d) are taken. (c) Shows an epitaxial grain and (d) shows an epitaxial layer with an edge dislocation which is further illustrated in the insert. Selected area diffraction pattern measured at the substrate-film interface in (e) region A and (f) region B.

relaxed. The spacing of the periodic dislocations corresponds with the 13.2 nm average periodicity of the additional Bragg reflections observed by the synchrotron XRD (Figure 5). Indicating that the relaxation of stress in the film by arrays of dislocations could give rise to the diffuse scattering observed by XRD. One of the dislocations from Figure 6(b) (marked "1") is shown in more detail in Figure 6 (c), where the lines illustrate the edge location that arises from the termination of a substrate lattice plane at the film interface. The selected area diffraction pattern in Figure 6(d) shows diffraction from a single $BaTiO_3$ crystallite, further demonstrating the cube-on-cube relationship between the film and substrate.

Multi-layered $BaTiO_3$ films on (100)-STO made by the same heating program as the film in Figure 6, but with the maximum annealing temperature being 700 °C instead of 1000 °C, were polycrystalline (Film 8). A cross-section of such a film is shown in Figure 7(a), where the thickness of the film was 193 nm giving 13 nm on average per deposited layer. The interface between the film and substrate in region A is shown in Figure 7(b). At the interface there was a cube-on-cube layer with a thickness of a few nm, but occasionally this (100)-orientation extended into grains grown from the substrate interface (Figure 7(c)). Edge dislocations were observed in the cube-on-cube layer caused by termination of substrate lattice

planes (Figure 7(d)), similar to the periodic dislocations observed for the (100)-oriented multilayer film (Film 7, Figure 6). Selected area diffraction patterns of the multilayer polycrystalline film in regions A and B are shown in Figure 7(e) and (f), respectively. The diffraction patterns did not show full diffraction rings for the $BaTiO_3$ film, indicating some degree of preferential orientation, at least close to the substrate interface.

2.4. Ferroelectric Characterization

The in-plane ferroelectric properties of the multilayer $BaTiO_3$ thin films on (100)STO are shown in Figure 8 along with the microstructure of the films. Both the polarization versus electrical field (P-E-loop) and the capacitance versus electric field (C-E-loop), reveal that only the film heated fast to a final annealing temperature of 1000 °C (Film 6) displayed ferroelectric switching. This is the same film that was characterized with TEM (Figure 6) and found to be highly (100)-oriented, caused by cube-on-cube growth. Neither of the multilayer films annealed at 700 °C showed polarization switching (Film 8 and Film 9), which could be a consequence of the fine-grained microstructure or an out-of-plane polarization axis. Multilayered BCT and BCZT films were also prepared by fast heating to 1000 °C, and the in-plane ferroelectric response was measured (Figure S7 in Supporting Information). However, the cation substituted films showed P-E-loops dominated by leakage, which likely is caused by the reduced thickness of these films compared to the $BaTiO_3$ film, as the film thickness is known to have major influence on the ferroelectric response.[13]

3. Discussion

3.1. Tailoring the Heating Program for Texture and Cube-on-Cube Growth

For a given precursor chemistry, the most important aspect to consider for annealing the oxide thin films from aqueous CSD is the heating profile used. The heating program will govern the thermal decomposition of the precursor and the crystallization process for the film, which in turn will decide the degree of preferred orientation, microstructure, strain and, hence, the functional properties of the resulting film. By adjusting the heating profile, the degree of preferred orientation in the films can be tailored. Figure 9(a) schematically illustrates the different regions of a heating program, where in Region 1 the thermal decomposition, organic burn-out and pyrolysis occurs, dependent on the precursor chemistry. Region 2 is the temperature range where nucleation and growth of the desired oxide film occurs and in Region 3 cube-on-cube growth is possible. However, this is highly dependent on the thermal history of the film, as these films do not necessarily follow classical nucleation and growth theory. In general, it is advantageous to fully crystallize each layer to ensure phase purity and limit cation segregation, dependent on the precursor chemistry. For the $BaTiO_3$ thin films made by the aqueous CSD method reported in this work, the parameters indicated in Figure 9(a) are as follows; the time in Region 1 t_{R1} = 2–10 min, the temperature limit between Region 1 and 2 $T_{R1/R2}$ = 550 °C and between Region 2 and 3 $T_{R2/R3}$ = 1000 °C. The hold time at the maximum annealing temperature depends slightly on the thickness of the deposited layer, however, 5 min was observed to be sufficient by the in situ XRD investigation, as the crystallinity of the films did not change significantly by further extending the annealing time.

If each layer is fully crystallized before depositing the next, highly oriented cube-on-cube grown films are possible. These films follow the substrate orientation for the single layered films (Figure 3 and Figure 4) as shown by XRD and by TEM for multilayered films (Figure 6). This step is illustrated in Fig-

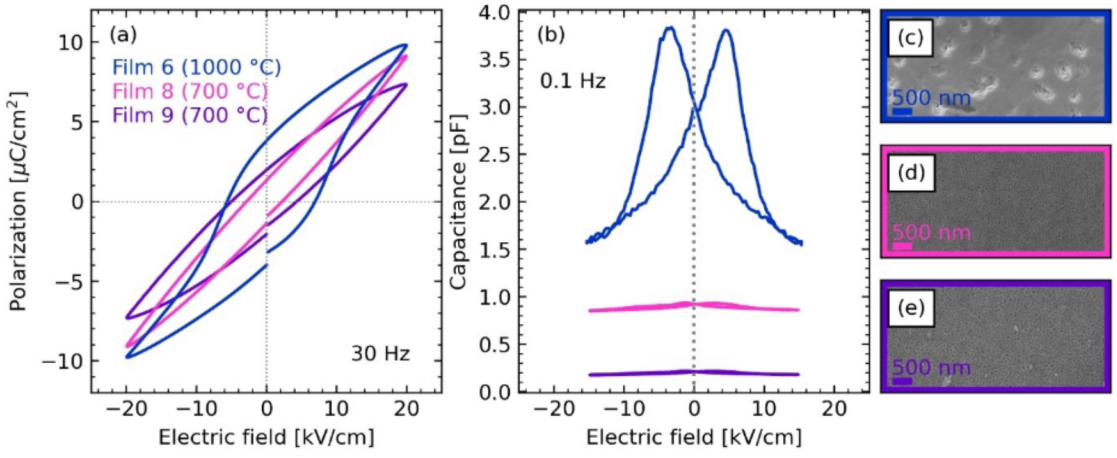

Figure 8. (a) Polarization and (b) capacitance versus electrical field loops for multilayer $BaTiO_3$ films on (100)-STO. Microstructure (top view) of the films, where

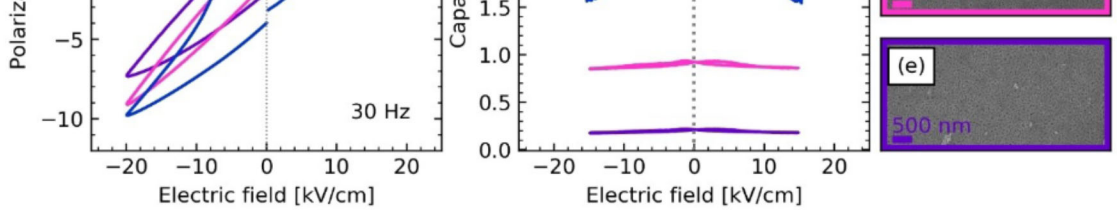

Figure 8. (a) Polarization and (b) capacitance versus electrical field loops for multilayer $BaTiO_3$ films on (100)-STO. Microstructure (top view) of the films, where (c) was heated slowly to 700 °C, (d) was heated fast to 700 °C and (e) was heated fast to 1000 °C.

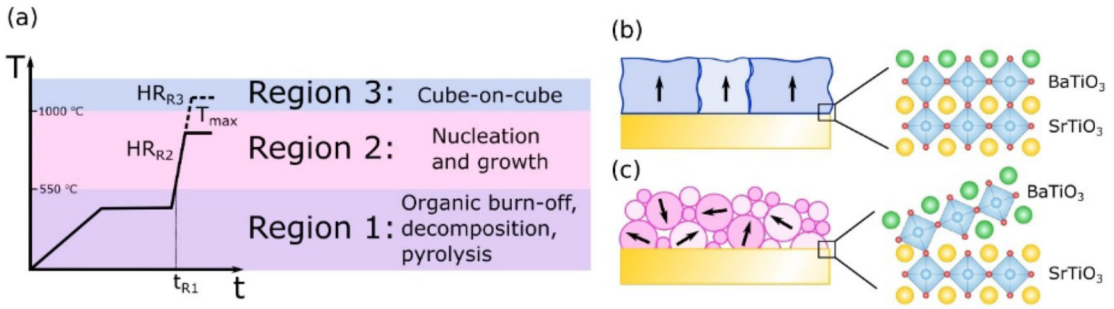

Figure 9. (a) Schematic division of the different regions occurring during annealing of thin films from CSD. The heating program should be designed based on the precursor chemistry governing Region 1 and the desired degree of preferential orientation, which is decided by the temperature-time (T-t) profile in Region 2 and Region 3. For the $BaTiO_3$ thin films made by the aqueous CSD method in this work, the parameters indicated are as follows; the time in Region 1 $t_{R1} = 2–10$ min, the temperature limit between Region 1 and 2 $T_{R1/R2} = 550\,°C$ and between Region 2 and 3 $T_{R2/R3} = 1000\,°C$. (b) Cube-on-cube growth giving a very high degree of preferred orientation in the film is only favourable in Region 3. (c) Polycrystalline films nucleate from annealing in Region 2. However, preferred orientation can be introduced by a sufficiently low heating rate (HR_{R2}) in Region 2.

ure 9(b). To achieve cube-on-cube growth with a very high degree of preferred orientation, the nucleation in the film must be limited before crossing the temperature threshold to where cube-on-cube growth is favoured. In a material system with homogenous nucleation, such as the $BaTiO_3$ films studied in this work,[14,16] a high heating rate HR_{R2} and HR_{R3} is necessary to kinetically limit the amount of nucleation and growth that can occur in Region 2 (as seen from the resulting diffraction of the films in Figure 3). Limiting the crystallization and growth until a high enough temperature is reached and the threshold for where cube-on-cube growth is favourable is crossed is crucial for achieving this high degree of preferred orientation. The annealing temperature T_{max} should be in Region 3, preferably 20–50 °C above the cube-on-cube threshold. For cube-on-cube growth the heating program in Region 1 is less significant, but still sufficient time should be chosen to allow for organic burnout and decomposition to avoid violent gas evolution at higher temperatures. For the $BaTiO_3$ films in this work the heating rates HR_{R2} and HR_{R3} should be in the range 5–20 °C s^{-1}, and $T_{max} > 1000\,°C$. Multilayer films are realised by repeating the same recommended heating program, as the previous layer will serve as a template for the consecutive deposited layers.

Textured $BaTiO_3$ films from aqueous CSD has been shown to arise from two different mechanisms. For single layer films, the texture is introduced by allowing sufficient time for the intermediate phases to orient according to the substrate, by designing a heating program that allow a long time in Region 1,[14] either by slow heating or by introducing a hold step just below the nucleation threshold (boundary between Region 1 and Region 2). The degree of preferred orientation was also reported to increase with a low heating rate through nucleation, meaning the heating program for the $BaTiO_3$ should have a high t_{R1} (5–10 min), a low HR_{R2} ($< 0.2\,°C\,s^{-1}$) and an annealing temperature $T_{max} > 650\,°C$.[14] However, such an annealing scheme is time consuming. The TEM imaging (Figure 7 and Figure S8 in the Supporting Information) also shows that texture can be induced by Ostwald ripening during the repeated deposition process. These multilayer films had an (100)-oriented layer at the substrate interface, which formed during the first annealing, since highly oriented reflections can be seen in the textured and polycrystalline single layered films investigated by in situ XRD.[14] The (100)-oriented layer is only a few nm thick (Figure 7 and Figure S8 in the Supporting Information), but epitaxial grains were also observed. The grains extend further into the film than the thickness of the first deposited layer, demonstrating increased orientation and that cube-on-cube grains grow from the substrate as constitutive layers are annealed. However, the maximum temperature is too low to enable the extensive grain growth associated with the final stage of the densification of the film. Moreover, cube-on-cube growth only occurs in a thin layer at the substrate interface or in grains grown from the substrate as the temperatures are not sufficient to overcome grain boundaries.[24] Preparation of textured multilayer films can therefore be achieved even with a heating program that does not result in textured single layers. For the $BaTiO_3$ films in this work, sufficient time in Region 1 is necessary, and $T_{max} > 650\,°C$ is beneficial, but a significantly higher heating rate in Region 2 can be used HR_{R2} ($< 20\,°C\,s^{-1}$) compared to textured single layers.

As previously reported, polycrystalline $BaTiO_3$ films with no preferred orientation requires fast heating.[14] A film as illustrated in Figure 9(c) and for a single layer, can be achieved by a high heating rate in Region 2 (3–20 °C s^{-1}) and a final annealing temperature also in Region 2, but for improved crystallinity $T_{max} > 650\,°C$ is recommended.[14] Additionally, sufficient time in Region 1 to allow complete organic burnout/precursor decomposition is necessary, where the heating rate and possible hold steps in this Region should be chosen based on the precursor chemistry and possible secondary phases. For the $BaTiO_3$ films in this work, it is irrelevant if t_{R1} is achieved by slow heating or fast heating and a hold step for the crystallinity, but it has been reported that for dense microstructure slow heating is beneficial to avoid holes in the film caused by gas evolution.[14] To achieve polycrystalline multilayer $BaTiO_3$ films from aqueous CSD, each layer should only be pyrolyzed and not heated into Region 2, due to texture induced by repeated annealing. Instead, each layer should be annealed at a temperature (in

Region 1) high enough to remove most of the organics, but low enough to avoid nucleation. Then a final annealing step for crystallization should be carried out with a high heating rate (3–20 °C s^{-1} and a final annealing temperature in Region 2, where for the $BaTiO_3$ films this means $T_{max} > 650$ °C for improved crystallinity. The same increase in crystallinity with higher annealing temperature in Region 2 was also reported in BCZT films based on the same aqueous precursor solutions.[17]

An important final note regarding the influence of the heating programs on the texture formation and cube-on-cube growth in the films reported in this work, is that they do not follow classical nucleation and growth theory, due to the chemistry of the aqueous precursor solutions. As a consequence, the processing parameters reported to give texture and epitaxy in more traditional $BaTiO_3$-based solutions with organic solvents,[3a,25] does not yield the same results for the aqueous solutions reported in this work. Demonstrating the importance of the precursor chemistry and the reactions occurring during the burn-out and decomposition stage (Region 1).

3.2. Substrate and Cation Substitution Effect on Crystallization

A requirement for film cube-on-cube growth is that the substrate has a compatible crystal lattice. STO and LAO are both perovskites, and the lattice mismatch related to $BaTiO_3$ is 2.6 and 5.4% respectively. MgO has cubic structure where the lattice mismatch is 4.9%. $BaTiO_3$ films on MgO and LAO were prepared with fast heating to 1000 °C, where the diffraction patterns (Figure S5 and Figure S6 in Supporting Information, respectively) indicated cube-on-cube growth in the films, however, the orientation is incomplete, resulting in a partial polycrystalline character. The BCT film prepared with fast heating to 1000 °C had the same microstructure as $BaTiO_3$, while the BCZT had a rougher appearance, possibly due to the annealing temperature (Figure S4(e) in Supporting Information). These films demonstrated that that cube-on-cube growth was possible on all the crystalline substrates investigated in this work, but complete transformation of the $BaTiO_3$ films was only possible on STO, which likely was due to temperature limitations on the heating setup. Since $BaTiO_3$ and STO are the most similar of the material systems and substrates investigated, the cube-on-cube growth threshold for $BaTiO_3$ on STO could be lower than $BaTiO_3$ on LAO, MgO and Pt/Si, or BCZT on STO. Therefore, it is proposed that complete epitaxial transformation can be achieved by increasing the annealing temperature. Although, in the case of using Pt/Si as a substrate there is an upper temperature limit reported below the cube-on-cube growth threshold, for which interactions with the Pt-layer and Si diffusion into the film deteriorate the ferroelectric properties.[24] Although cube-on-cube growth can be achieved, the high temperatures necessary could cause other issues for film fabrication. Moreover, the mechanisms for texture formation in the $BaTiO_3$-based films, was observed to not be impacted the kinetics of texture formation. Therefore, the mechanisms described for $BaTiO_3$ films, can also be expected in other $BaTiO_3$-based films from aqueous CSD.

3.3. Lattice Parameters and Relaxation in Cube-on-Cube Grown Films

In Section 2.2, the lattice parameter for a cube-on-cube grown single layer $BaTiO_3$ film on STO (Film 6, Figure 4), was calculated from the (300)-, (310)- and (311)-reflections, where the (300)- and (310)-reflections gave significantly lower pseudo-cubic lattice parameters then the (311)-reflection. The (300)- and (310)-reflections have a larger contribution from lattice planes parallel to the substrate surface and are therefore a good indication of the in-plane lattice parameter, which shows how the film is compressively strained from the substrate. The lattice parameter calculated from (311) was larger, as these lattice planes also have a contribution from the out-of-plane parameter, which fits with the expansion compensating for the in-plane compressive strain. In contrast, multilayer relaxed epitaxial 180 nm thick $BaTiO_3$ films from the same aqueous CSD synthesis route as presented in this work were also prepared by Ræder et al.[13] The lattice parameters of multilayer $BaTiO_3$ films were found to be 4.010 Å in-plane and 4.000 Å out-of-plane,[13] which contrasts with the parameters found in this work for the 25 nm film (Film 6, Figure 4). Ræder et al. concluded that the c-axis was in-plane, giving rise to in-plane polarization caused by the mismatch in thermal expansion coefficients between $BaTiO_3$ and the STO substrates.[13] During cooling from the annealing temperature (1000 °C) the film is clamped to the substrate, which induces tensile strain in the film. Since the same experimental procedure and a similar heating programs were used in this work as by Ræder et al., the same polarization state and strain situation can be assumed for the multilayer films reported in this work. The contrasting in-plane and out-of-plane lattice parameters reported here for a single layer film and by Ræder et al. for multilayered films might be an effect of different degree of relaxation as the film thickness is a factor of 10 larger for the multilayer films. The incomplete coverage seen for the single layer films in this work (Figure 3) could also alter the strain state of the film compared to the multilayer films, as the boundary conditions of the films would differ as a result of the degree of coverage.

The TEM imaging revealed that the multilayer cube-on-cube grown films had periodic dislocations at the substrate interface (Figure 6). The periodicity of the dislocations (14.0 nm) from TEM is close to the distance predicted based on full relaxation of stress from the lattice mismatch (16.2 nm) and the average periodicity (13.3 nm) from the additional reflections observed by synchrotron XRD for a single layer relaxed epitaxial film (Figure 5). It is therefore proposed that the additional reflections seen by synchrotron XRD are due to the periodic dislocations arising from relaxation of the film due to mismatch in lattice parameters, meaning that the dislocations are highly ordered and formed during crystallization of the first deposited layer.

ature. Although, in the case of using Pt/Si as a substrate there is an upper temperature limit reported below the cube-on-cube growth threshold, for which interactions with the Pt-layer and Si diffusion into the film deteriorate the ferroelectric properties.[24] Although cube-on-cube growth can be achieved, the high temperatures necessary could cause other issues for film fabrication. Moreover, the mechanisms for texture formation in the $BaTiO_3$-based films, was observed to not be impacted by cation substitution, although zirconium significantly reduced

of stress from the lattice mismatch (16.2 nm) and the average periodicity (13.3 nm) from the additional reflections observed by synchrotron XRD for a single layer relaxed epitaxial film (Figure 5). It is therefore proposed that the additional reflections seen by synchrotron XRD are due to the periodic dislocations arising from relaxation of the film due to mismatch in lattice parameters, meaning that the dislocations are highly ordered and formed during crystallization of the first deposited layer. Similar reflection objects have been observed in relation to

ferroelectric domain pattern in other materials.[27] However, in the present work, these reflections were observed at significantly higher temperatures than the expected Curie temperature of the films,[13,15a] and therefore cannot be caused by diffuse scattering from the ferroelectric domains.

3.4. The Influence of Texture on the Ferroelectric Properties of the $BaTiO_3$-based Thin Films

The ferroelectric properties of the $BaTiO_3$-based thin films were highly dependent on the microstructure and degree of preferential orientation, but the remnant polarizations and coercive fields were in the same range as typically reported for $BaTiO_3$ films from CSD.[6b,7,26,28] Only the cube-on-cube grown films gave an open hysteresis loop, while the response from the polycrystalline multilayer films made by fast and slow heating to 700 °C was nearly linear. The grain sizes of the polycrystalline films are in the range of the critical grain sizes observed in literature,[2b] which could contribute to the limited ferroelectric response. Moreover, the slim capacitance versus electric field (C-E-loops) measured for these films (Figure 8(b)) have also been reported for polycrystalline $BaTiO_3$ films on LAO made by a CSD process, where the ferroelectric response was measured with interdigitated electrodes.[29] Dimos et al. observed an increased tunability when the annealing temperature was higher as this increased the grain sizes in the polycrystalline film, but the C-E-loops remained slim.[29]

The limited in-plane response from the polycrystalline films, could also be due to different orientation of the polar axis (c-axis) in these films, giving less in-plane response. The TEM investigation (Figure 7 and Figure S8 in Supporting Information) only shows that these films have a preferred orientation, but this does not need to be conforming to the substrate orientation. As these films were less clamped by the substrate contraction during the fabrication, which Ræder et al. reported to be responsible for the in-plane polarization,[13] a different preferred orientation could occur.

3.5. The Advantages of in situ X-ray Diffraction in Combination with TEM Imaging

The work presented in this paper demonstrates the deeper understanding that can be obtained by in situ studies of the reactions occurring during annealing of $BaTiO_3$-based thin films from aqueous chemical solution deposition. The in situ XRD measurements were crucial in revealing the impact of the heating program on both microstructure and texture development in the films. Moreover, the in situ XRD studies conducted in this work revealed conditions must be met to achieve cube-on-cube growth. The cube-on-cube grown films have been characterized previously by TEM,[15] but the origin of this growth mode has not been reported. The in situ XRD also demonstrated how texture developed in the films and the orientation relationship between the film and substrate in single layer films, and the effect of cation substitution and substrate had on the texture formation. However, by combining the in situ measurements with TEM of multilayer films, the effect of repeated annealing on furthered development of preferred orientation in the films was shown. Furthermore, the combination of in situ XRD studies with TEM was important not only for understanding the transformation pathway in the $BaTiO_3$-based thin films, but also for proposing a more generalised scheme for how the processing parameters can be altered to tailor the thin films (Figure 9). This generalized model can serve as a guide for fabrication of thin film with preferred orientation of other related material systems by CSD.

4. Conclusion

The crystallization process of textured and cube-on-cube grown $BaTiO_3$-based thin films from aqueous chemical solution deposition was characterized by in situ synchrotron X-ray diffraction and transmission electron microscopy. The in situ analysis revealed the conditions required for achieving cube-on-cube growth in the $BaTiO_3$-based films, and it is proposed that the mechanisms could be valid for other oxide thin films as well. The crystallographic texture in the films were characterized and demonstrated to adhere to the substrate orientation. Guidelines for how the thermal annealing of $BaTiO_3$-based thin films should be designed for achieving different degrees of preferred orientation in the films were outlined. Moreover, the relaxation of stress in the films was demonstrated to depend on the number of deposited layers (film thickness/coverage), where the main source of stress is the thermal annealing procedure. The ferroelectric characterization showed that only the cube-on-cube grown films have in-plane ferroelectric response.

Acknowledments

Financial support from NTNU and The Research Council of Norway under the Toppforsk program to the project (250403) "From Aqueous Solutions to oxide Thin films and hierarchical Structures" (FASTS) is gratefully acknowledged. The Research Council of Norway is also acknowledged for the support to the Norwegian Micro- and Nano-Fabrication Facility, NorFab, (245963/F50) and the Norwegian Center for Transmission Electron Microscopy, NORTEM (197405/F50). Finally, we acknowledge the SNX council for allocation of the beamtimes at the Swiss-Norwegian Beamline (SNBL) synchrotron facilities at the ESRF (The European Synchrotron Radiation Facility, Grenoble, France) and the SNBL beamline staff for their support during the experiments.

Conflict of Interest

The authors declare no conflict of interest.

Keywords: aqueous synthesis · $BaTiO_3$ thin films · crystallization · in situ X-ray diffraction · texture

[1] G. H. Haertling, *J. Vac. Sci. Technol. A* **1991**, *9*, 414–420.
[2] a) J. Rodel, W. Jo, K. T. P. Seifert, E. M. Anton, T. Granzow, D. Damjanovic, *J. Am. Ceram. Soc.* **2009**, *92*, 1153–1177; b) M. Acosta, N. Novak, V. Rojas, S. Patel, R. Vaish, J. Koruza, G. A. Rossetti, J. Rodel, *Appl. Phys.* **2017**, *4*.
[3] a) R. W. Schwartz, T. Schneller, R. Waser, *C. R. Chim.* **2004**, *7*, 433–461; b) N. Bassiri-Gharb, Y. Bastani, A. Bernal, *Chem. Soc. Rev.* **2014**, *43*, 2125–2140.
[4] T. Mitsui, W. B. Westphal, *Phys. Rev.* **1961**, *124*, 1354–1359.
[5] W. Liu, X. Ren, *Phys. Rev. Lett.* **2009**, *103*, 257602.
[6] a) R. Ashiri, A. Nemati, M. S. Ghamsari, M. M. Dastgahi, *J. Mater. Sci. Mater. Electron.* **2014**, *25*, 5345–5355; b) S. Halder, T. Schneller, R. Waser, *J. Sol-Gel Sci. Technol.* **2005**, *33*, 299–306; c) U. Hasenkox, S. Hoffmann, R. Waser, *J. Sol-Gel Sci. Technol.* **1998**, *12*, 67–79; d) S. Hoffmann, R. Waser, *J. Eur. Ceram. Soc.* **1999**, *19*, 1339–1343; e) R. W. Schwartz, P. G. Clem, J. A. Voigt, E. R. Byhoff, M. Van Stry, T. J. Headley, N. A. Missert, *J. Am. Ceram. Soc.* **1999**, *82*, 2359–2367; f) L. N. Gao, J. W. Zhai, X. Yao, *J. Sol-Gel Sci. Technol.* **2008**, *45*, 51–55.
[7] J. P. George, J. Beeckman, W. Woestenborghs, P. F. Smet, W. Bogaerts, K. Neyts, *Nanoscale Res. Lett.* **2013**, *8*, 62.
[8] T. Hosokura, A. Ando, T. Konoike, *RSC Adv.* **2015**, *5*, 97563–97567.
[9] B. I. Edmondson, S. Kwon, C. H. Lam, J. E. Ortmann, A. A. Demkov, M. J. Kim, J. G. Ekerdt, *J. Am. Ceram. Soc. 2020, 103,1209–1218.*
[10] M. J. Choi, J. R. Lim, J. S. Choi, J. H. Eom, B. J. Park, K. S. Kim, D. Kim, S. G. Yoon, *Scr. Mater.* **2015**, *108*, 96–99.
[11] B. C. Luo, D. Y. Wang, M. M. Duan, S. Li, *Appl. Phys. Lett.* **2013**, *103*, 122903.
[12] a) Y. Chen, T. Y. Zhang, Q. G. Chi, J. Q. Lin, X. Wang, Q. Q. Lei, *J. Alloys Compd.* **2016**, *663*, 818–822; b) W. Li, J. Hao, H. Zeng, J. Zhai, *Curr. Appl. Phys.* **2013**, *13*, 1205–1208; c) W. L. Li, T. D. Zhang, D. Xu, Y. F. Hou, W. P. Cao, W. D. Fei, *J. Eur. Ceram. Soc.* **2015**, *35*, 2041–2049; d) M. Shi, J. G. Zhong, R. Z. Zuo, Y. D. Xu, L. Wang, H. L. Su, C. Gu, *J. Alloys Compd.* **2013**, *562*, 116–122.
[13] T. M. Raeder, K. Bakken, J. Glaum, M. A. Einarsrud, T. Grande, *AIP Adv.* **2018**, *8*.
[14] K. Bakken, A. B. Blichfeld, D. Chernyshov, T. Grande, J. Glaum, M.-A. Einarsrud, *J. Sol-Gel Sci. Technol.* **2020**, *95*, 562–572.
[15] a) T. M. Raeder, T. S. Holstad, I.-E. Nylund, M.-A. Einarsrud, J. Glaum, D. Meier, T. Grande, *AIP Adv.* **2021**, *11*, 025016; b) I.-E. Nylund, T. M. Raeder, P. E. Vullum, T. Grande, *J. Appl. Phys.* **2021**, *129*, 095304.
[16] K. Bakken, V. H. Pedersen, A. B. Blichfeld, I.-E. Nylund, S. Tominaka, K. Ohara, T. Grande, M.-A. Einarsrud, *ACS Omega* **2021**, *6*, 9567–9576.
[17] E. Khomyakova, S. Wenner, K. Bakken, J. Schultheiß, T. Grande, J. Glaum, M.-A. Einarsrud, *J. Eur. Ceram. Soc.* **2020**, *40*, 5376–5383.
[18] A. B. Blichfeld, K. Bakken, D. Chernyshov, J. Glaum, T. Grande, M.-A. Einarsrud, *J. Synchrotron Radiat.* **2020**, *27*, 1209–1217.
[19] V. Dyadkin, P. Pattison, V. Dmitriev, D. Chernyshov, *J. Synchrotron Radiat.* **2016**, *23*, 825–829.
[20] D. Chernyshov, V. Dyadkin, W. van Beek, A. Urakawa, *Acta Crystallogr. Sect. A* **2016**, *72*, 500–506.
[21] L. Lutterotti, *Nucl. Instrum. Methods Phys. Res., Sect. B* **2010**, *268*, 334–340.
[22] a) R. Hielscher, H. Schaeben, *J. Appl. Crystallogr.* **2008**, *41*, 1024–1037; b) F. Bachmann, R. Hielscher, H. Schaeben, *Solid State Phenom.* **2010**, *160*, 63–68.
[23] T. M. Reader, U. Hanke, E. Halvorsen, T. Grande, *Smart Mater. Struct.* **2020**, *29*, 8.
[24] D. W. Richerson, Modern ceramic engineering : properties, processing, and use in design, Vol. 29, 3rd ed., CRC Press, Boca Raton, Fla, **2006**.
[25] A. Queralto, M. de la Mata, J. Arbiol, X. Obradors, T. Puig, *Adv. Mater. Interfaces* **2016**, *3*, 1600392.
[26] T. M. Stawski, W. J. C. Vijselaar, O. F. Gobel, S. A. Veldhuis, B. F. Smith, D. H. A. Blank, J. E. ten Elshof, *Thin Solid Films* **2012**, *520*, 4394–4401.
[27] E. Wintersberger, N. Hrauda, D. Kriegner, M. Keplinger, G. Springholz, J. Stangl, G. Bauer, J. Oswald, T. Belytschko, C. Deiter, F. Bertram, O. H. Seeck, *Appl. Phys. Lett.* **2010**, *96*, 131905.
[28] D. S. Paik, A. V. P. Rao, S. Komarneni, *J. Sol-Gel Sci. Technol.* **1997**, *10*, 213–220.
[29] D. Dimos, M. V. Raymond, R. W. Schwartz, H. N. Al-Shareef, C. H. Mueller, *J. Electroceram.* **1997**, *1*, 145–153.

Manuscript received: July 19, 2021
Version of record online: October 14, 2021